APSIPA Transactions on Signal and Information Processing, 2025, 14, e28

Original Paper

Spatial Active Noise Control Based on Kernel Interpolation With Individual Directional Weighting

Kazuyuki Arikawa[1], Shoichi Koyama[2*] and Hiroshi Saruwatari[1]

[1] *The University of Tokyo, Tokyo 113-8656, Japan.*
[2] *National Institute of Informatics, Tokyo 101-8430, Japan.*

ABSTRACT

An active noise control (ANC) method for reducing noise over a region in space based on the individual kernel interpolation of primary and secondary sound fields is proposed. The kernel-interpolation-based spatial ANC based on the estimation and synthesis of a three-dimensional sound field using multiple microphones and secondary sources has practical advantages in an arbitrary array configuration and efficient time-domain algorithms. It is possible to incorporate prior information on primary noise source directions into the kernel function by directional weighting to enhance the estimation accuracy of a sound field; however, in a previous study, the performance improvement by this directional weighting is limited owing to the mismatch of the source direction in the sound field generated by secondary sources. We propose a spatial ANC method based on the individual interpolation of the sound fields generated by primary and secondary sources. An adaptive filtering algorithm for individual kernel interpolation is also developed. The experimental results indicate that the proposed method outperforms the previous kernel-interpolation-based spatial ANC.

*Corresponding author: koyama.shoichi@ieee.org. This work was supported by JST FOREST Program, Grant Number JPMJFR216M.

Received 26 May 2025; revised 10 July 2025; accepted 12 August 2025
ISSN 2048-7703; DOI 10.1561/116.20250034

Keywords: Adaptive filter, spatial active noise control, kernel ridge regression, interpolation

1 Introduction

Active noise control (ANC) is a technique of suppressing incoming primary noise by generating antinoise with secondary sources. In general feedforward ANC techniques, the driving signals of the secondary sources are obtained by applying an adaptive filter, which is updated on the basis of the residual noise captured by error microphones, to reference microphone signals. ANC has been investigated for many years from both theoretical and practical aspects [8, 19, 15, 11, 5, 20, 14].

Spatial ANC is aimed at attenuating noise over a three-dimensional (3D) space, where multiple microphones and secondary sources are used to capture and synthesize a 3D sound field. Conventional multipoint pressure control techniques are limited to reducing noise in the vicinity of the error microphone positions because the cost function for updating the driving signals of the secondary sources is usually defined as the power of the error microphone signals [8]. In recent spatial ANC techniques, reducing noise over a 3D target region is achieved by estimating and synthesizing a continuous sound field based on the spherical/circular harmonic expansion [26, 4, 16, 21] or kernel interpolation [9, 12]. In particular, the spatial ANC technique based on kernel interpolation for sound fields has practical advantages in the applicability of arbitrary array configuration and efficient time-domain adaptive filtering algorithms. Unlike many virtual sensing techniques [17], another advantage is that no prior identification stage to estimate the filter for predicting virtual error signals from physical ones are required.

The kernel-interpolation-based spatial ANC is based on the sound field estimation using the reproducing kernel function that constrains the interpolated function satisfying the homogeneous Helmholtz equation in the frequency domain [24, 23]. Thus, the cost function defined as the acoustic potential energy in the target region is computed from the error microphone signals. An adaptive filtering algorithm based on filtered-x least mean squares (FxLMS) for feedforward spatial ANC is also derived in [12]. Although the kernel function includes a directional weighting function to enhance the estimation accuracy for sound fields generated by given source directions [23], the case of uniform weighting, where the possible primary noise source directions are assumed to be uniform, is investigated in [9, 12]. However, in some practical situations, it is possible to assume that approximate directions of primary noise sources are available. To incorporate this prior information, a kernel function with directional weighting on the primary noise source direction is applied in [10]. It is shown that the interpolation accuracy, as well as regional noise reduction

performance, can be improved by appropriately setting parameters for the directional weighting, compared with the method using uniform weighting.

An issue in the previous study in [10] is that the directional weighting on the primary noise source direction is applied to interpolate the residual noise field, or the *total sound field*, from the error microphone signals. The total sound field is essentially a superposition of sound fields generated by the primary noise source (*primary sound field*) and secondary sources (*secondary sound field*). Since the secondary sources are typically placed in different directions from the primary noise source, it is inappropriate to simply apply the directional weighting on the primary noise source direction when interpolating the total sound field. That is the reason why the improvement of regional noise reduction is still limited in [10]. We hereafter refer to this interpolation procedure as *total kernel interpolation*.

To overcome the issue in the total kernel interpolation, we propose *individual kernel interpolation*. Specifically, we individually interpolate the primary and secondary sound fields using kernel interpolation with the directional weighting on each primary/secondary source direction and estimate the total sound field as a sum of the two sound fields. The directions of the secondary sources can also be given in many practical spatial ANC systems. By separately dealing with the primary and secondary sound fields, we can expect further improvement in the interpolation accuracy of the total sound field. Preliminary results of the individual kernel interpolation in the frequency domain are reported in [3]. In this paper, we also derive an FxLMS algorithm based on the individual kernel interpolation for adaptive filtering in the time domain.

The rest of this paper is organized as follows. In Section 2, the problem formulation of the spatial ANC is described. In Section 3, the kernel interpolation of sound fields with directional weighting, as well as the kernel-interpolation-based spatial ANC technique, is introduced. The proposed individual kernel interpolation is described in Section 4, and the FxLMS algorithm based on the individual kernel interpolation is also developed in this section. In Section 5, experimental results to evaluate the proposed method are reported. Finally, Section 6 concludes this paper.

1.1 Notation

The sets of real and complex numbers are denoted by $\mathbb{R}$ and $\mathbb{C}$, respectively. The unit sphere in $\mathbb{R}^3$ is denoted by $\mathbb{S}_2$. The imaginary unit is denoted by j ($\mathrm{j}^2 := -1$). The complex conjugate is denoted by the superscript $(\cdot)^*$. The transpose, conjugate transpose, and inverse of a matrix are denoted by the superscripts $(\cdot)^{\mathsf{T}}$, $(\cdot)^{\mathsf{H}}$, and $(\cdot)^{-1}$, respectively. The Frobenius norm of a matrix $\boldsymbol{A}$ is denoted by $\|\boldsymbol{A}\|_F$ and $\otimes$ denotes the Kronecker product. The identity matrix of size $N \times N$ is denoted by $\boldsymbol{I}_N$.

The angular frequency and the sound speed are denoted by ω and c, respectively. The wave number is denoted by $k := \omega/c$. The harmonic time dependence $\mathrm{e}^{\mathrm{j}\omega t}$ with the time t is assumed throughout this paper.

2 Problem Formulation

Suppose that secondary sources (or secondary loudspeakers) are placed inside or near the boundary of a target region $\Omega \subset \mathbb{R}^3$, as shown in Figure 1. The goal of spatial ANC is to reduce incoming primary noise over Ω by emitting antinoise signals. Our particular interest here is the use of prior knowledge about the directions of the primary noise sources and/or secondary sources to enhance the performance of spatial ANC. Reference microphones are typically placed between primary noise sources and Ω to capture primary noise before it reaches Ω. Error microphones are placed inside or near the boundary of Ω to obtain the residual noise. The driving signals of the secondary sources are updated using an adaptive filtering algorithm based on the microphone signals. Hereafter, we denote the numbers of reference microphones, secondary sources, and error microphones as R, L, and M, respectively.

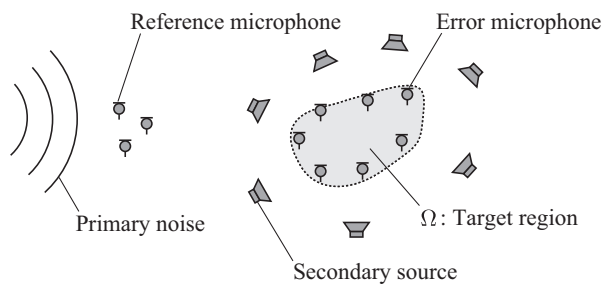

Figure 1: Feedforward spatial ANC system using reference and error microphones and secondary sources.

The signals of the reference microphones and secondary sources at the discrete time index n are denoted as $\boldsymbol{x}(n) \in \mathbb{R}^R$ and $\boldsymbol{y}(n) \in \mathbb{R}^L$, respectively. The signals of error microphones and the primary noise at positions of error microphones are denoted as $\boldsymbol{e}(n) \in \mathbb{R}^M$ and $\boldsymbol{d}(n) \in \mathbb{R}^M$, respectively. The total sound field, i.e., the sum of primary and secondary sound fields, at the position $\boldsymbol{r} \in \Omega$ and time n is denoted as $u_\mathrm{t}(\boldsymbol{r}, n)$. When using pressure microphones, the mth element of $\boldsymbol{e}(n)$, denoted as $e_m(n)$, is equivalent to the pressure u_t at the position of the mth error microphone $\boldsymbol{r}_m$, i.e., $e_m(n) = u_\mathrm{t}(\boldsymbol{r}_m, n)$, except for sensor noise. Furthermore, the primary and secondary sound fields are denoted as $u_\mathrm{p}(\boldsymbol{r}, n)$ and $u_\mathrm{s}(\boldsymbol{r}, n)$, respectively. We also denote signals in

the frequency domain using the angular frequency ω as an argument. For instance, the reference microphone signal in the frequency domain is denoted as $\boldsymbol{x}(\omega)$.

The impulse responses between the secondary sources and error microphones, i.e., secondary paths, are represented by the multiple-input multiple-output (MIMO) finite impulse response (FIR) filter $\boldsymbol{G}(j) \in \mathbb{R}^{M \times L}$ of length J, where each j refers to a matrix of filter coefficients. The error microphone signals $\boldsymbol{e}(n)$ can be represented as a superposition of the primary noise and the signals produced by secondary sources as

$$\boldsymbol{e}(n) = \boldsymbol{d}(n) + \sum_{j=0}^{J-1} \boldsymbol{G}(j)\boldsymbol{y}(n-j). \tag{1}$$

We assume that the true secondary paths are given by measuring or modeling them in advance. The control filter is the MIMO FIR filter $\boldsymbol{W}(i) \in \mathbb{R}^{L \times R}$ of length I. The driving signals of the secondary sources $\boldsymbol{y}(n)$ are computed by filtering the reference microphone signals $\boldsymbol{x}(n)$ with $\boldsymbol{W}(i)$ as

$$\boldsymbol{y}(n) = \sum_{i=0}^{I-1} \boldsymbol{W}(i)\boldsymbol{x}(n-i). \tag{2}$$

Here, we assume that the effect of secondary source signals at the reference microphone positions, i.e., *acoustic feedback*, is negligible. The effect of acoustic feedback can be mitigated by using directional loudspeakers [18] or by canceling acoustic feedback using the estimated acoustic feedback path [1]. The control filter $\boldsymbol{W}(i)$ is adaptively updated to minimize the total sound field inside Ω, namely, $u_{\mathrm{t}}(\boldsymbol{r}, n)$.

3 Spatial ANC Based on Kernel Interpolation of Total Sound Field

Prior work on spatial ANC based on the kernel interpolation of sound fields [12], which is the basis of our proposed method, is introduced. Since the objective of spatial ANC is to minimize the power of the total sound field inside Ω, we define the cost function to minimize in the adaptation process as the acoustic potential energy inside Ω as

$$\mathcal{L} := \mathbb{E}\left[\int_{\Omega} |u_{\mathrm{t}}(\boldsymbol{r}, n)|^2 \, \mathrm{d}\boldsymbol{r}\right], \tag{3}$$

where $\mathbb{E}[\cdot]$ represents the expectation operator. Here, we assume that the total sound field at time n, $u_{\mathrm{t}}(\boldsymbol{r}, n)$, is a weakly stationary process with respect to n. To calculate the cost function $\mathcal{L}$ in (3), it is necessary to obtain the continuous total sound field $u_{\mathrm{t}}(\boldsymbol{r}, n)$.

3.1 Kernel Interpolation of Sound Fields

In [12], kernel ridge regression is applied to estimate the total sound field in the frequency domain, $u_{\mathrm{t}}(\cdot, \omega)$, at each frequency. Let $\mathcal{H}(\omega) = \{u(\cdot, \omega) : \mathbb{R}^3 \mapsto \mathbb{C}\}$ be a reproducing kernel Hilbert space in which the solution for $u_{\mathrm{t}}(\cdot, \omega)$ is searched. Specifically, $\mathcal{H}(\omega)$ consists of Herglotz wave functions [6] (or plane wave decomposition), represented as

$$u(\boldsymbol{r}, \omega) = \frac{1}{4\pi} \int_{\mathbb{S}_2} \tilde{u}(\boldsymbol{\xi}) \mathrm{e}^{\mathrm{j}k\boldsymbol{\xi}^{\mathsf{T}}\boldsymbol{r}} \, \mathrm{d}\boldsymbol{\xi}, \tag{4}$$

where $\tilde{u}(\boldsymbol{\xi})$ is the square-integrable complex amplitude of the plane wave of the arrival direction, $\boldsymbol{\xi} \in \mathbb{S}_2$. Furthermore, the positive-definite reproducing kernel $\kappa(\cdot, \cdot, \omega) : \mathbb{R}^3 \times \mathbb{R}^3 \mapsto \mathbb{C}$ for $\mathcal{H}(\omega)$ is represented as

$$\kappa(\boldsymbol{r}_1, \boldsymbol{r}_2, \omega) = \frac{1}{4\pi} \int_{\mathbb{S}_2} \gamma(\boldsymbol{\xi}) \mathrm{e}^{\mathrm{j}k\boldsymbol{\xi}^{\mathsf{T}}(\boldsymbol{r}_1 - \boldsymbol{r}_2)} \, \mathrm{d}\boldsymbol{\xi}. \tag{5}$$

Here, $\gamma(\cdot) : \mathbb{S}_2 \mapsto \mathbb{R}_{\geq 0}$ is a weighting function. In kernel ridge regression, $u_{\mathrm{t}}(\cdot, \omega) \in \mathcal{H}(\omega)$ is estimated from the error microphone signals at the angular frequency ω as

$$u_{\mathrm{t}}(\boldsymbol{r}, \omega) = \boldsymbol{z}_e(\boldsymbol{r}, \omega)^{\mathsf{T}} \boldsymbol{e}(\omega) \tag{6}$$

with the interpolation filter

$$\boldsymbol{z}_e(\boldsymbol{r}, \omega) := \left[(\boldsymbol{K}(\omega) + \lambda \boldsymbol{I}_M)^{-1} \right]^{\mathsf{T}} \boldsymbol{\kappa}(\boldsymbol{r}, \omega), \tag{7}$$

where $\lambda > 0$ is a regularization parameter and $\boldsymbol{K}(\omega) \in \mathbb{C}^{M \times M}$ and $\boldsymbol{\kappa}(\boldsymbol{r}, \omega) \in \mathbb{C}^M$ are the Gram matrix and the vector consisting of the kernel function, represented as

$$\boldsymbol{K}(\omega) := \begin{bmatrix} \kappa(\boldsymbol{r}_1, \boldsymbol{r}_1, \omega) & \cdots & \kappa(\boldsymbol{r}_1, \boldsymbol{r}_M, \omega) \\ \vdots & \ddots & \vdots \\ \kappa(\boldsymbol{r}_M, \boldsymbol{r}_1, \omega) & \cdots & \kappa(\boldsymbol{r}_M, \boldsymbol{r}_M, \omega) \end{bmatrix}, \tag{8}$$

$$\boldsymbol{\kappa}(\boldsymbol{r}, \omega) := \begin{bmatrix} \kappa(\boldsymbol{r}, \boldsymbol{r}_1, \omega) & \cdots & \kappa(\boldsymbol{r}, \boldsymbol{r}_M, \omega) \end{bmatrix}^{\mathsf{T}}. \tag{9}$$

Again, $\boldsymbol{r}_m$ denotes the position of the mth error microphone. The estimated sound field $u_{\mathrm{t}}(\boldsymbol{r}, \omega)$ in (6) is guaranteed to satisfy the homogeneous Helmholtz equation.

3.2 Kernel Function with Directional Weighting

The weighting function $\gamma(\cdot)$ in (5) is used to incorporate prior knowledge on sound source directions. Suppose that the arrival direction of a single primary

noise source $\boldsymbol{\eta}$ is given. In [23], the von Mises–Fisher distribution is used as the weighting function, defined as

$$\gamma(\boldsymbol{\xi}) := \mathrm{e}^{\beta \boldsymbol{\eta}^{\mathsf{T}} \boldsymbol{\xi}}, \tag{10}$$

where $\beta \geq 0$ is a weighting parameter for controlling the sharpness of the weighting on the direction $\boldsymbol{\eta}$. If β is set large, the estimated total sound field $u_{\mathrm{t}}(\cdot, \omega)$ is supposed to have a large gain in the direction $\boldsymbol{\eta}$. By substituting (10) into (5), we can represent the kernel function with directional weighting as

$$\kappa(\boldsymbol{r}_1, \boldsymbol{r}_2, \omega) = j_0 \left(\sqrt{(\mathrm{j}\beta\boldsymbol{\eta} - k\boldsymbol{r}_{12})^{\mathsf{T}} (\mathrm{j}\beta\boldsymbol{\eta} - k\boldsymbol{r}_{12})} \right). \tag{11}$$

Here, $\boldsymbol{r}_{12} := \boldsymbol{r}_2 - \boldsymbol{r}_1$ and $j_0(\cdot)$ is the 0th-order spherical Bessel function of the first kind. It is reported in [10] that a larger noise power reduction can be achieved by appropriately setting the parameter β than by using the uniform weight $\gamma(\boldsymbol{\xi}) = 1$ (i.e., $\beta = 0$) in experiments in the frequency domain.

3.3 FxLMS Algorithm Based on Total Kernel Interpolation

To derive the FxLMS algorithm to minimize the cost function in (3), $u_{\mathrm{t}}(\cdot, n)$ is obtained by the inverse discrete-time Fourier transform of $u_{\mathrm{t}}(\cdot, \omega)$ as

$$\begin{aligned} u_{\mathrm{t}}(\boldsymbol{r}, n) &= \mathcal{F}^{-1} \left[u_{\mathrm{t}}(\boldsymbol{r}, \omega) \right](n) \\ &= \sum_{i=-\infty}^{\infty} \boldsymbol{z}_e(\boldsymbol{r}, i)^{\mathsf{T}} \boldsymbol{e}(n-i), \end{aligned} \tag{12}$$

where $\boldsymbol{z}_e(\boldsymbol{r}, i) := \mathcal{F}^{-1}[\boldsymbol{z}_e(\boldsymbol{r}, \omega)](i)$ is the interpolation filter in the time domain. By substituting (12) into (3), we can represent the gradient of $\mathcal{L}$ with respect to the filter coefficients $\boldsymbol{W}(i)$ as

$$\begin{aligned} \boldsymbol{\Delta}(i) &:= \frac{1}{2} \frac{\partial \mathcal{L}}{\partial \boldsymbol{W}(i)} \\ &= \sum_{k=-\infty}^{\infty} \sum_{j=0}^{J-1} \boldsymbol{G}(j)^{\mathsf{T}} \boldsymbol{A}(k)^{\mathsf{T}} \boldsymbol{R}_{ex}(i+j+k). \end{aligned} \tag{13}$$

Here, $\boldsymbol{R}_{ex}(j) := \mathbb{E}[\boldsymbol{e}(n)\boldsymbol{x}(n-j)^{\mathsf{T}}]$ is the cross correlation between the error and reference microphone signals, and it is assumed to be dependent only on the time difference j. $\boldsymbol{A}(k)$ is the weighting filter matrix obtained by the inverse Fourier transform of $\boldsymbol{A}(\omega)$, which is defined as

$$\boldsymbol{A}(\omega) := \int_{\Omega} \boldsymbol{z}_e(\boldsymbol{r}, \omega)^* \boldsymbol{z}_e(\boldsymbol{r}, \omega)^{\mathsf{T}} \, \mathrm{d}\boldsymbol{r}. \tag{14}$$

Here, $\boldsymbol{A}(\omega)$ can be computed offline usually by numerical integration. Furthermore, the weighting filter matrix $\boldsymbol{A}(k)$ is approximated by a causal FIR filter of length $2K+1$, $\hat{\boldsymbol{A}}(k)$, which is obtained by truncating $\boldsymbol{A}(k)$ within $-K \leq k \leq K$ and by adding a delay of K samples. By replacing the cross correlation $\boldsymbol{R}_{ex}(\cdot)$ with the instantaneous value at time n, we can finally obtain the FxLMS algorithm based on kernel interpolation as

$$\boldsymbol{W}_{n+1}(i) = \boldsymbol{W}_n(i) - \mu_n \hat{\boldsymbol{\Delta}}_n(i) \tag{15}$$

with the approximated gradient at time n

$$\hat{\boldsymbol{\Delta}}_n(i) = \sum_{k=0}^{2K} \sum_{j=0}^{J-1} \boldsymbol{G}(j)^{\mathsf{T}} \hat{\boldsymbol{A}}(k)^{\mathsf{T}} \boldsymbol{e}(n-K) \boldsymbol{x}(n-i-j-k)^{\mathsf{T}}. \tag{16}$$

Here, the same delay K is added to the error signal $\boldsymbol{e}$, and μ_n is the normalized step size obtained as

$$\mu_n = \frac{\mu_0}{\sum_i \| \sum_j \boldsymbol{G}(j) \otimes \boldsymbol{x}(n-i-j) \|_F^2 + \epsilon}, \tag{17}$$

where $\mu_0 > 0$ is a constant step-size parameter and $\epsilon > 0$ is a regularization parameter for avoiding zero division. The approximated gradient (16) can be equivalently represented as

$$\hat{\boldsymbol{\Delta}}_n(i) = \sum_{k=0}^{J+2K-1} \boldsymbol{H}(k)^{\mathsf{T}} \boldsymbol{e}(n-K) \boldsymbol{x}(n-i-k)^{\mathsf{T}}, \tag{18}$$

where $\boldsymbol{H}(k)$ is the linear convolution of $\hat{\boldsymbol{A}}(k)$ and $\boldsymbol{G}(j)$ computed as

$$\boldsymbol{H}(k) := \sum_{j=0}^{2K} \hat{\boldsymbol{A}}(j) \boldsymbol{G}(k-j). \tag{19}$$

We also note that the update rule of conventional FxLMS for multipoint pressure control [8] is represented as

$$\boldsymbol{W}_{n+1}(i) = \boldsymbol{W}_n(i) - \mu_n \sum_{j=0}^{J-1} \boldsymbol{G}(j)^{\mathsf{T}} \boldsymbol{e}(n) \boldsymbol{x}(n-i-j)^{\mathsf{T}}, \tag{20}$$

which can be obtained by skipping the convolution of $\hat{\boldsymbol{A}}(i)$ in (16).

4 Spatial ANC Based on Individual Kernel Interpolation

As we described in Section 3.2, prior information on the primary noise source direction can be incorporated into the interpolation procedure with the directional weighting function (10). However, the improvement in ANC performance compared with the case of using the uniform weight ($\gamma(\boldsymbol{\xi}) = 1$) is

still limited. The main issue with the current interpolation procedure is that the total sound field u_t is interpolated with the directional weighting only on the primary noise source direction $\boldsymbol{\eta}$. The total sound field u_t is essentially a superposition of the primary sound field u_p and the secondary sound field u_s. Nevertheless, a single interpolation filter, $\boldsymbol{z}_e$, which consists of the kernel function weighted on the primary noise source direction, is applied to estimate u_t as

$$\begin{aligned} u_\mathrm{t}(\boldsymbol{r},\omega) &= u_\mathrm{p}(\boldsymbol{r},\omega) + u_\mathrm{s}(\boldsymbol{r},\omega) \\ &= \boldsymbol{z}_e(\boldsymbol{r},\omega)^\mathsf{T}\boldsymbol{d}(\omega) + (\boldsymbol{G}(\omega)^\mathsf{T}\boldsymbol{z}_e(\boldsymbol{r},\omega))^\mathsf{T}\boldsymbol{y}(\omega), \end{aligned} \tag{21}$$

where $\boldsymbol{d}(\omega)$, $\boldsymbol{y}(\omega)$, and $\boldsymbol{G}(\omega)$ are the Fourier transforms of $\boldsymbol{d}(n), \boldsymbol{y}(n)$, and $\boldsymbol{G}(n)$, respectively. However, the secondary sources generating u_s are not usually in the same direction as the primary noise source, as can be seen in Figure 1. This *directional mismatch* limits the interpolation accuracy of the previous method; therefore, the improvement in ANC performance is also limited. We refer to the interpolation procedure in (21) as the total kernel interpolation. We also refer to the FxLMS algorithm introduced in Section 3.3 as the total-kernel-interpolation-based FxLMS algorithm (Total-KI-FxLMS).

4.1 Individual Kernel Interpolation of Sound Fields

The issue with total kernel interpolation is that the secondary sound field is interpolated with the kernel function weighted on the primary noise source direction. Therefore, following our previous work [3], we formulate the individual kernel interpolation as

$$\begin{aligned} u_\mathrm{t}(\boldsymbol{r},\omega) &= u_\mathrm{p}(\boldsymbol{r},\omega) + u_\mathrm{s}(\boldsymbol{r},\omega) \\ &= \boldsymbol{z}_d(\boldsymbol{r},\omega)^\mathsf{T}\hat{\boldsymbol{d}}(\omega) + \boldsymbol{\zeta}_y(\boldsymbol{r},\omega)^\mathsf{T}\boldsymbol{y}(\omega). \end{aligned} \tag{22}$$

Here, $\hat{\boldsymbol{d}}(\omega)$ is the estimated primary noise component in error microphone signals estimated as

$$\hat{\boldsymbol{d}}(\omega) = \boldsymbol{e}(\omega) - \boldsymbol{G}(\omega)\boldsymbol{y}(\omega). \tag{23}$$

The vectors $\boldsymbol{z}_d(\cdot,\omega)$ and $\boldsymbol{\zeta}_y(\cdot,\omega)$ are interpolation filters for the primary and secondary sound fields, respectively. The interpolation filter $\boldsymbol{z}_d(\cdot,\omega)$ is obtained using (7) with the kernel function with directional weighting on the primary noise source direction $\boldsymbol{\eta}$, and the weighting parameter β_d. If we set the weighting parameter to be the same as that in the total kernel interpolation, it holds that $\boldsymbol{z}_d(\cdot,\omega) = \boldsymbol{z}_e(\cdot,\omega)$. In contrast, the secondary sound field

u_s is estimated for each secondary source as

$$\begin{aligned} u_\mathrm{s}(\boldsymbol{r},\omega) &= \sum_{l=1}^{L} \boldsymbol{z}_{y,l}(\boldsymbol{r},\omega)^\mathsf{T} \boldsymbol{G}_l(\omega) y_l(\omega) \\ &= \left[\boldsymbol{G}_1(\omega)^\mathsf{T} \boldsymbol{z}_{y,1}(\boldsymbol{r},\omega), \cdots, \boldsymbol{G}_L(\omega)^\mathsf{T} \boldsymbol{z}_{y,L}(\boldsymbol{r},\omega)\right] \boldsymbol{y}(\omega), \end{aligned} \tag{24}$$

where $\boldsymbol{G}_l(\omega)$ is the lth column of $\boldsymbol{G}(\omega)$ and $\boldsymbol{z}_{y,l}(\cdot,\omega)$ is the interpolation filter given by (7) with the direction of the lth secondary source $\boldsymbol{\eta}_l$ and the weighting parameter β_l to compute the kernel function in (11). Therefore, $\boldsymbol{\zeta}_y$ in (22) is calculated as

$$\boldsymbol{\zeta}_y(\boldsymbol{r},\omega) = \left[\boldsymbol{G}_1(\omega)^\mathsf{T} \boldsymbol{z}_{y,1}(\boldsymbol{r},\omega), \cdots, \boldsymbol{G}_L(\omega)^\mathsf{T} \boldsymbol{z}_{y,L}(\boldsymbol{r},\omega)\right]^\mathsf{T}. \tag{25}$$

4.2 Individual-kernel-interpolation-based FxLMS Algorithm

We derive an FxLMS algorithm on the basis of the individual kernel interpolation in the same manner as in Section 3.3. The total sound field in the time domain $u_\mathrm{t}(\cdot,n)$ is obtained by the inverse Fourier transform of $u_\mathrm{t}(\cdot,\omega)$ in (22) as

$$u_\mathrm{t}(\boldsymbol{r},n) = \sum_{i=-\infty}^{\infty} \left[\boldsymbol{z}_d(\boldsymbol{r},i)^\mathsf{T} \hat{\boldsymbol{d}}(n-i) + \boldsymbol{\zeta}_y(\boldsymbol{r},i)^\mathsf{T} \boldsymbol{y}(n-i)\right]. \tag{26}$$

Here, $\boldsymbol{z}_d(\cdot,i)$ and $\boldsymbol{\zeta}_y(\cdot,i)$ are the interpolation filters in the time domain, which are calculated by the inverse Fourier transform of $\boldsymbol{z}_d(\cdot,\omega)$ and $\boldsymbol{\zeta}_y(\cdot,\omega)$, respectively. By substituting (26) into (3), we can obtain the gradient of $\mathcal{L}$ with respect to the filter coefficients $\boldsymbol{W}(i)$ as

$$\begin{aligned} \boldsymbol{\Delta}(i) = &\sum_{k=-\infty}^{\infty} \boldsymbol{A}_{dy}(k)^\mathsf{T} \boldsymbol{R}_{ex}(i+k) \\ &+ \sum_{k=-\infty}^{\infty} \boldsymbol{A}_{ydy}(k)^\mathsf{T} \boldsymbol{R}_{yx}(i+k), \end{aligned} \tag{27}$$

where $\boldsymbol{R}_{yx}(j) := \mathbb{E}\left[\boldsymbol{y}(n)\boldsymbol{x}(n-j)^\mathsf{T}\right]$ is the cross correlation between the driving signals and the reference microphone signals. The matrices $\boldsymbol{A}_{dy}(k)$ and $\boldsymbol{A}_{ydy}(k)$ are the weighting filter matrices obtained by the inverse Fourier transform of $\boldsymbol{A}_{dy}(\omega)$ and $\boldsymbol{A}_{ydy}(\omega)$, which are computed as

$$\boldsymbol{A}_{dy}(\omega) := \int_\Omega \boldsymbol{z}_d(\boldsymbol{r},\omega)^* \boldsymbol{\zeta}_y(\boldsymbol{r},\omega)^\mathsf{T} \,\mathrm{d}\boldsymbol{r} \tag{28}$$

$$\boldsymbol{A}_{ydy}(\omega) := \int_\Omega \boldsymbol{\zeta}_y(\boldsymbol{r},\omega)^* \boldsymbol{\zeta}_y(\boldsymbol{r},\omega)^\mathsf{T} \,\mathrm{d}\boldsymbol{r} - \boldsymbol{G}(\omega)^\mathsf{H} \boldsymbol{A}_{dy}(\omega). \tag{29}$$

These matrices can be computed offline. Furthermore, we approximate $\boldsymbol{A}_{dy}(k)$ with the causal FIR filter $\hat{\boldsymbol{A}}_{dy}(k)$, which is obtained by truncating $\hat{\boldsymbol{A}}_{dy}(k)$ within $-K \leq k \leq K+J-1$ and by adding a delay of K samples. In the same manner, $\boldsymbol{A}_{ydy}(k)$ is approximated with $\hat{\boldsymbol{A}}_{ydy}(k)$, which is obtained by the truncation of $\boldsymbol{A}_{ydy}(k)$ within $-K \leq k \leq K$ and by a delay of K samples. By substituting $\boldsymbol{R}_{ex}(\cdot)$ and $\boldsymbol{R}_{yx}(\cdot)$ in (27) with instantaneous values at time n, we can derive the approximated gradient at time n as

$$\hat{\boldsymbol{\Delta}}_n(i) = \sum_{k=0}^{J+2K-1} \hat{\boldsymbol{A}}_{dy}(k)^{\mathsf{T}} \boldsymbol{e}(n-K)\boldsymbol{x}(n-i-k)^{\mathsf{T}} + \sum_{k=0}^{2K} \hat{\boldsymbol{A}}_{ydy}(k)^{\mathsf{T}} \boldsymbol{y}(n-K)\boldsymbol{x}(n-i-k)^{\mathsf{T}}. \tag{30}$$

We note that the filter length of $\hat{\boldsymbol{A}}_{dy}(k)$, $J+2K$, is selected to be the same as the length of $\boldsymbol{H}(k)$ in (18). $\hat{\boldsymbol{\Delta}}_n(i)$ is used to update the control filter using (15), with the step size μ_n defined in (17). We refer to the update rule described above as the individual-kernel-interpolation-based FxLMS algorithm (Individual-KI-FxLMS).

4.3 Comparison with Total-KI-FxLMS Algorithm

We describe the relationships between the previous method (Total-KI-FxLMS) and the proposed method (Individual-KI-FxLMS). Figure 2 shows the block diagrams of the two methods. Total-KI-FxLMS computes the cross correlation between the error microphone signals and the filtered reference microphone signals, whereas Individual-KI-FxLMS additionally computes the cross correlation between the driving signals and the filtered reference microphone signals. The additional term, which is the second term in (30), can be viewed as a *correction term* for modifying the gradient of the control filter.

We show that the correction term becomes zero and that Individual-KI-FxLMS becomes identical to Total-KI-FxLMS in a certain case. Suppose that the kernel functions for computing $\boldsymbol{z}_d(\cdot,\omega)$ and $\boldsymbol{\zeta}_y(\cdot,\omega)$ are the same with the same parameters $\boldsymbol{\eta}$ and β. In this case, by substituting $\boldsymbol{z}_{y,l}(\cdot,\omega) = \boldsymbol{z}_d(\cdot,\omega)$ $(\forall l \in \{1,\cdots,L\})$ into (25), we can represent $\boldsymbol{\zeta}_y(\cdot,\omega)$ as

$$\begin{aligned}\boldsymbol{\zeta}_y(\boldsymbol{r},\omega) &= \left[\boldsymbol{G}_1(\omega)^{\mathsf{T}}\boldsymbol{z}_d(\boldsymbol{r},\omega),\cdots,\boldsymbol{G}_L(\omega)^{\mathsf{T}}\boldsymbol{z}_d(\boldsymbol{r},\omega)\right]^{\mathsf{T}} \\ &= \boldsymbol{G}(\omega)^{\mathsf{T}}\boldsymbol{z}_d(\boldsymbol{r},\omega).\end{aligned} \tag{31}$$

Therefore, the first term in (29) becomes

$$\begin{aligned}\int_\Omega \boldsymbol{\zeta}_y(\boldsymbol{r},\omega)^*\boldsymbol{\zeta}_y(\boldsymbol{r},\omega)^{\mathsf{T}}\,\mathrm{d}\boldsymbol{r} &= \boldsymbol{G}(\omega)^{\mathsf{H}}\left(\int_\Omega \boldsymbol{z}_d(\boldsymbol{r},\omega)^*\boldsymbol{\zeta}_y(\boldsymbol{r},\omega)^{\mathsf{T}}\,\mathrm{d}\boldsymbol{r}\right) \\ &= \boldsymbol{G}(\omega)^{\mathsf{H}}\boldsymbol{A}_{dy}(\omega),\end{aligned} \tag{32}$$

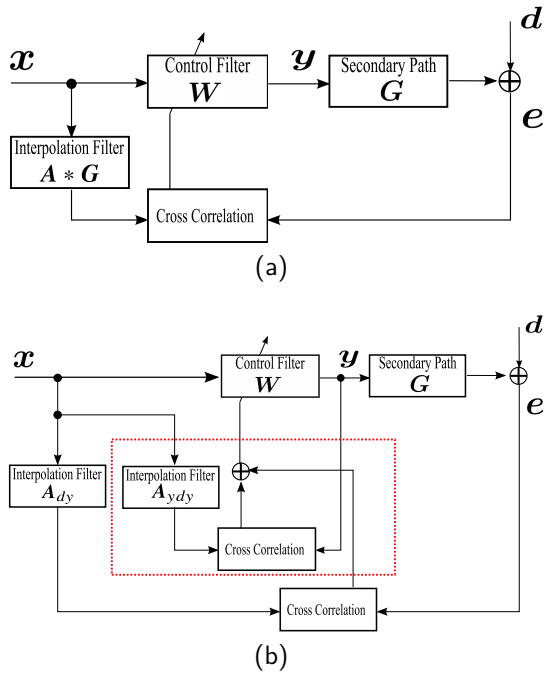

Figure 2: Block diagrams of (a) Total-KI-FxLMS and (b) Individual-KI-FxLMS algorithms. The red dotted rectangle in (b) indicates the blocks differentiating the two methods.

which readily leads to $\boldsymbol{A}_{ydy}(\omega) = \boldsymbol{0}$ $(\forall\omega)$. Furthermore, if we set the weighting parameter used in $\boldsymbol{z}_d(\cdot,\omega)$ to be the same as that in $\boldsymbol{z}_e(\cdot,\omega)$, i.e., $\boldsymbol{z}_d(\cdot,\omega) = \boldsymbol{z}_e(\cdot,\omega)$, $\boldsymbol{A}_{dy}(\omega)$ is represented as

$$\begin{aligned}\boldsymbol{A}_{dy}(\omega) &= \left(\int_\Omega \boldsymbol{z}_d(\boldsymbol{r},\omega)^* \boldsymbol{z}_d(\boldsymbol{r},\omega)^\mathsf{T}\,\mathrm{d}\boldsymbol{r}\right)\boldsymbol{G}(\omega)\\ &= \left(\int_\Omega \boldsymbol{z}_e(\boldsymbol{r},\omega)^* \boldsymbol{z}_e(\boldsymbol{r},\omega)^\mathsf{T}\,\mathrm{d}\boldsymbol{r}\right)\boldsymbol{G}(\omega)\\ &= \boldsymbol{A}(\omega)\boldsymbol{G}(\omega). \end{aligned} \tag{33}$$

Finally, by substituting $\boldsymbol{A}_{dy}(k) = \mathcal{F}^{-1}[\boldsymbol{A}_{dy}(\omega)](k) = \mathcal{F}^{-1}[\boldsymbol{A}(\omega)\boldsymbol{G}(\omega)](k)$ and $\boldsymbol{A}_{ydy}(k) = \mathcal{F}^{-1}[\boldsymbol{A}_{ydy}(\omega)](k) = \boldsymbol{0}$ into (27), we can represent the gradient (before approximation) for Individual-KI-FxLMS as

$$\begin{aligned}\boldsymbol{\Delta}(i) &= \sum_{k=-\infty}^{\infty}\sum_{j=0}^{J-1}\boldsymbol{G}(j)^{\mathsf{T}}\boldsymbol{A}(k-j)\boldsymbol{R}_{ex}(i+k)\\ &= \sum_{k'=-\infty}^{\infty}\sum_{j=0}^{J-1}\boldsymbol{G}(j)^{\mathsf{T}}\boldsymbol{A}(k')\boldsymbol{R}_{ex}(i+j+k'),\end{aligned} \tag{34}$$

which is identical to the gradient for Total-KI-FxLMS in (13). Here, we apply a change in variable $k' = k - j$ to derive (34). From the above discussion, we can consider Individual-KI-FxLMS as a generalization of Total-KI-FxLMS.

We also discuss the difference in computational cost. The number of multiplications required to calculate the gradient of the cost function for every sample of the input signals is compared among conventional FxLMS, Total-KI-FxLMS, and Individual-KI-FxLMS in Table 1. The computational cost for Individual-KI-FxLMS is the largest among the methods owing to the calculation of the additional second term in (30). The ratio of the computational cost for Individual-KI-FxLMS to that for Total-KI-FxLMS is

$$\begin{aligned}&\frac{RLM(I+J+2K)+RL^2(I+2K)}{RLM(I+J+2K)}\\ &\quad= 1+\frac{I+2K}{I+J+2K}\frac{L}{M}.\end{aligned} \tag{35}$$

The number of secondary sources, L, is typically set to less than the number of error microphones, M; therefore, the computational cost for Individual-KI-FxLMS is less than double that for Total-KI-FxLMS.

Table 1: Computational Complexities of Algorithms

Algorithm	Number of multiplications
FxLMS	$RLM(I+J)$
Total-KI-FxLMS	$RLM(I+J+2K)$
Individual-KI-FxLMS	$RLM(I+J+2K)+RL^2(I+2K)$

5 Experiments

Numerical experiments were conducted to evaluate the performance of the proposed Individual-KI-FxLMS in comparison with that of the previous Total-KI-FxLMS. In Sections 5.1 and 5.2, the ANC performance of the methods under different settings was investigated. In Section 5.3, the experimental results obtained using the real data measured using a practical array system are shown.

5.1 ANC Performance for Different Weighting Parameters

In both the Individual- and Total-KI-FxLMS algorithms, the weighting parameter β in the kernel function (10) plays an important role. We here investigate the performance of these methods at different weighting parameters in a simulated free-field or reverberant environment. For both methods, the weighting parameter was varied from 0.0 to 10.0 at 1.0 intervals. For the Individual-KI-FxLMS algorithm, the weighting parameters for interpolating the primary and secondary sound fields were kept the same. The integrals in (14), (28), and (29) were computed with naive Monte Carlo integration with 1000 samples. The regularization parameter for kernel ridge regression λ in (7) was set to 10^{-3}. The weighting filter matrices $\boldsymbol{A}(\omega)$, $\boldsymbol{A}_{dy}(\omega)$, and $\boldsymbol{A}_{ydy}(\omega)$ were computed at 4096 frequency bins with a sampling rate of 4000 Hz. The truncation length for the FIR filter was $K = 77$, which was chosen in line with the previous study in [12].

The room for simulation was a cuboid with dimensions of $7.5\,\mathrm{m} \times 5.0\,\mathrm{m} \times 2.5\,\mathrm{m}$. For the reverberant environment, the impulse responses were computed using the image source method [2] with a sampling rate of 4000 Hz. The three reverberation times T_{60} of 0.26 s, 0.65 s, and 1.39 s were investigated. We assumed that the true secondary path was given. As shown in Figure 3, the target region Ω was a cuboid with dimensions of $0.6\,\mathrm{m} \times 0.6\,\mathrm{m} \times 0.1\,\mathrm{m}$ with its center at the coordinate origin. The numbers of error microphones and secondary sources were set to $M = 16$ and $L = 12$, respectively. The secondary sources were regularly arranged on the borders of two squares with dimensions of $2.0\,\mathrm{m} \times 2.0\,\mathrm{m}$ at heights of $z = \pm 0.1$ m. The error microphones were regularly placed on the borders of the top and bottom squares of Ω, where every second microphone was shifted outwards by 0.03 m to alleviate the forbidden frequency problem [25, 13]. A single primary noise source was placed at $(-3.5,\ 0.4,\ 0.0)\,\mathrm{m}$. The primary noise was white Gaussian noise, filtered through a bandpass filter with a passband of 100–600 Hz. The reference microphone signal was directly obtained from the primary noise source. All the primary and secondary sources were point sources. White Gaussian noise was also added to the reference and error microphone signals so that the signal-to-noise ratio (SNR) was 40 dB.

To reduce the computational cost of the Individual- and Total-KI-FxLMS algorithms, we applied a fast block algorithm [12, 7] to both methods. In this method, the control filter is kept constant during a finite block, which allows us to update the control filter efficiently with the fast Fourier transform. The detailed procedure for updating the control filter with the fast block algorithm is described in [12, 7]. The block size B of the fast block algorithm was set to 3048. The length of the control filter, I, was also set to 3048. The regularization parameter ϵ in the step size (17) was 10^{-3}, and the normalized step-size parameter μ_0 was set to 20 for the free-field environment and 12 for

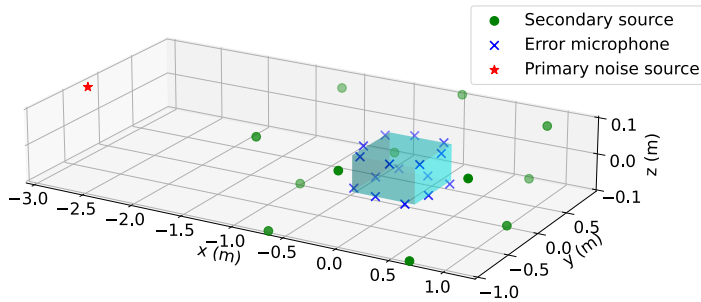

Figure 3: Positions of primary source (red star), secondary sources (green circles), and error microphones (blue crosses) in numerical experiments. The target region Ω is indicated by the blue cuboid.

the reverberant environment, which were experimentally selected so that the best performance was obtained.

As a performance measure for spatial ANC, we define the regional noise power reduction P_{red} as

$$P_{\mathrm{red}}(n) := 10\log_{10}\frac{\sum_j \sum_\nu u_{\mathrm{t}}(\boldsymbol{r}_j, n-\nu)^2}{\sum_j \sum_\nu u_{\mathrm{p}}(\boldsymbol{r}_j, n-\nu)^2}, \tag{36}$$

where u_{t} and u_{p} are the total and primary sound fields, respectively. The signal power is calculated over a window in time, $\nu \in [0, T-1]$ with $T = 2048$, and $\boldsymbol{r}_j$ is the jth evaluation point inside Ω. We placed 1024 evaluation points at regular intervals inside Ω. We note that a smaller P_{red} value indicates a higher performance in noise reduction. We also denote the average $P_{\mathrm{red}}(n)$ value for the last 30 s by $\bar{P}_{\mathrm{red}}$, which measures the regional noise reduction performance after the convergence of the control filter. The sampling rate for simulation was set to 4000 Hz and the control filter was updated for 750 s.

Figure 4 shows the $\bar{P}_{\mathrm{red}}$ values of Individual- and Total-KI-FxLMS for different weighting parameters. Figure 4a shows that the performance of Total-KI-FxLMS became worse with increasing the weighting parameter from 1.0 in the free-field environment. This is due to the problem of directional mismatch in the total kernel interpolation described in Section 4. Since individual kernel interpolation has resolved the problem of directional mismatch, Individual-KI-FxLMS achieved a higher performance when increasing the weighting parameter. Figures 4b, 4c, and 4d indicate that the highest performance of Individual-KI-FxLMS in the reverberant environment can be achieved by different weighting parameters depending on the reverberation time. If the weighting parameter is set to an excessively large value, the interpolated sound field will get closer to the direct sound field, which is not ap-

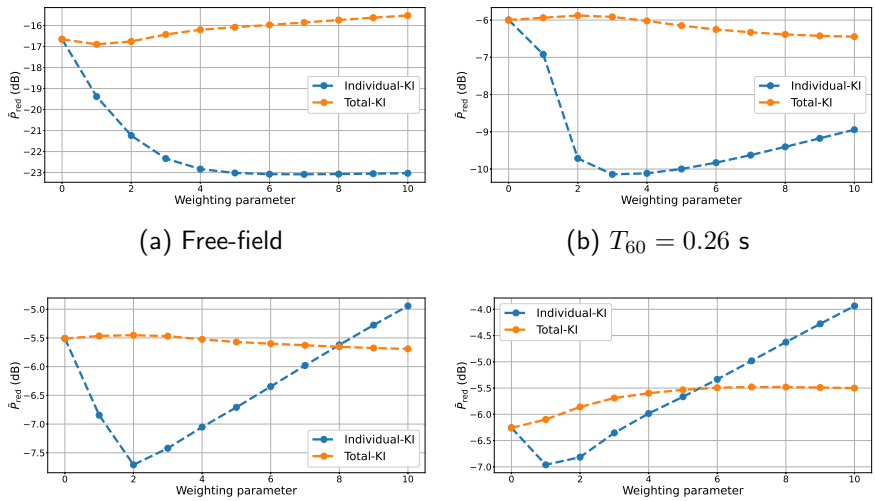

(a) Free-field (b) $T_{60} = 0.26$ s

(c) $T_{60} = 0.65$ s (d) $T_{60} = 1.39$ s

Figure 4: $\bar{P}_{\mathrm{red}}$ of Individual- and Total-KI-FxLMS algorithms as a function of the weighting parameter in (a) free-field and (b), (c), (d) reverberant environments.

propriate in a reverberant environment. Hence, setting a large weight for the source directions in kernel interpolation could deteriorate the interpolation accuracy. However, Individual-KI-FxLMS can still outperform Total-KI-FxLMS in terms of $\bar{P}_{\mathrm{red}}$ if the weighting parameter is appropriately selected.

Figure 5 shows P_{red} with respect to time under the free-field environment. The weighting parameters β for Individual- and Total-KI-FxLMS were set to 1.0 and 10.0, respectively. The power distribution on the horizontal plane at the height of 0.0 m after 750 s is shown in Figure 6. Although the noise reduction of Total-KI-FxLMS was evident only around the error microphones, Individual-KI-FxLMS achieved an almost uniform noise reduction in the entire target region owing to high interpolation accuracy.

We also investigate the ANC performance of the proposed method when different weighting parameters are used for interpolating the primary and secondary sound fields. We denote the weighting parameter in the interpolation filter $\boldsymbol{z}_d(\cdot, \omega)$, which is used for the interpolation of the primary sound field, as β_{p}. In the same manner, the weighting parameter in the interpolation filters, $\boldsymbol{z}_{y,l}(\cdot, \omega)$, which is used for the interpolation of the secondary sound field, is denoted as β_{s}. We assume that β_{s} is common for $\forall l \in \{1, \cdots, L\}$. The weighting parameters β_{p} and β_{s} were each varied from 0.0 to 10.0 at 2.0 intervals, and the same experiment as described above was performed. Figure 7 shows

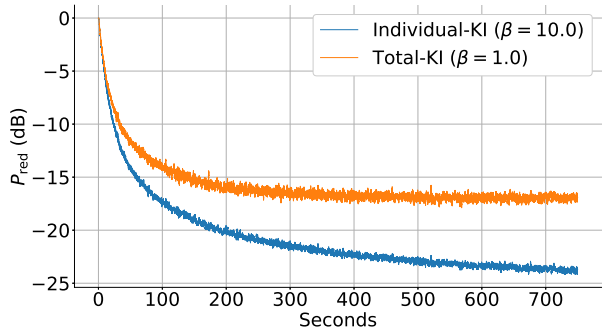

Figure 5: P_{red} values of Individual- and Total-KI-FxLMS with respect to time under the free-field environment.

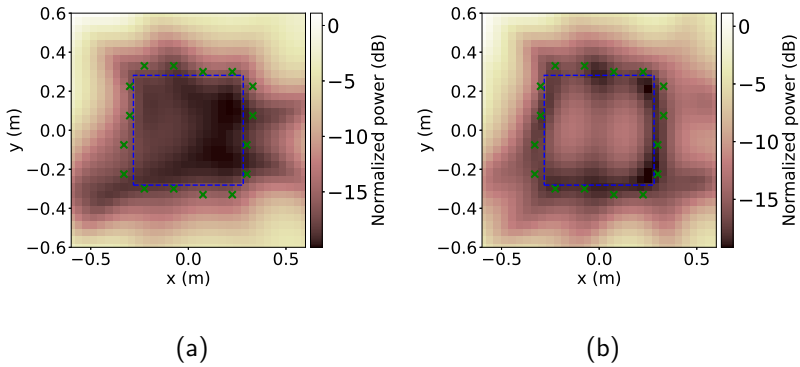

Figure 6: Power distribution in dB after 750 s achieved by (a) Individual- and (b) Total-KI-FxLMS under a free-field environment. The power is normalized by the average pressure of the primary sound field inside the square with dimensions of 0.6 m × 0.6 m. The blue dashed square is the border of the target region and the green crosses denote the error microphones.

$\bar{P}_{\mathrm{red}}$ achieved by the proposed method as a function of β_{p} and β_{s}. For the free-field environment, we can see that the noise reduction performance was improved by increasing both β_{p} and β_{s} (i.e., on a diagonal line in Figure 7a) because the kernel function tends to enhance the direct sounds by using large values of β_{p} and β_{s}. This result indicates that interpolating both the primary and secondary sound fields with high accuracy is important for higher noise reduction performance. For the reverberant environment, Figures 7b, 7c, and 7d show that the noise reduction performance depends on both β_{p} and β_{s}. For

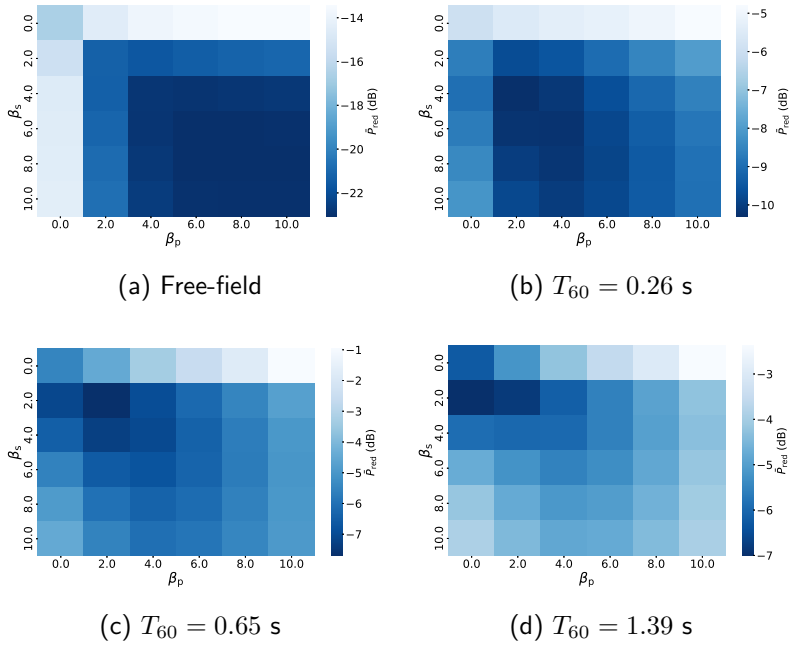

Figure 7: Relationship between $\bar{P}_{\mathrm{red}}$ achieved by Individual-KI-FxLMS and the weighting parameters (β_{p}, β_{s}) under (a) free-field and (b), (c), (d) reverberant environments.

example, the performance for T_{60} of 0.65 s became optimal when the weighting parameters were $\beta_{\mathrm{p}} = \beta_{\mathrm{s}} = 2.0$ and degraded with increasing β_{p} or β_{s}. Therefore, it is necessary to carefully choose the weighting parameters for the reverberant environment.

5.2 Robustness against Perturbation of Primary Noise Source and Secondary Source Positions

Both Individual- and Total-KI-FxLMS use the prior information of the primary noise source direction; furthermore, Individual-KI-FxLMS also uses the prior information of the secondary source direction. Therefore, it is valuable to investigate the robustness of the methods against the mismatch between the true and prior directions of the primary and secondary sources. First, the prior position of the primary noise source was fixed and perturbation was added to the position by using a Gaussian distribution of mean 0 and the standard deviations of 0.0 m, $\Delta\phi$ deg, and $\Delta\theta$ deg for its radial, azimuth, and zenith coordinates, respectively. We fixed one of $\Delta\phi$ and $\Delta\theta$ to 0.0 and selected the other from $\{0.0, 10.0, 20.0, 30.0\}$. We performed five independent

trials for each pair of $(\Delta\phi,\ \Delta\theta)$ under the free-field environment; therefore, we performed 40 $(= 5 \times 4 \times 2)$ trials in total. The other settings are the same as in the experiments in Section 5.1. Figure 8 shows the mean $\bar{P}_{\mathrm{red}}$ in each case with the standard deviation shown as error bars. It is clear that a larger perturbation added to the primary noise source position led to a worse noise reduction performance. However, the degree of decline in performance and the standard deviations among the trials were almost the same for both methods.

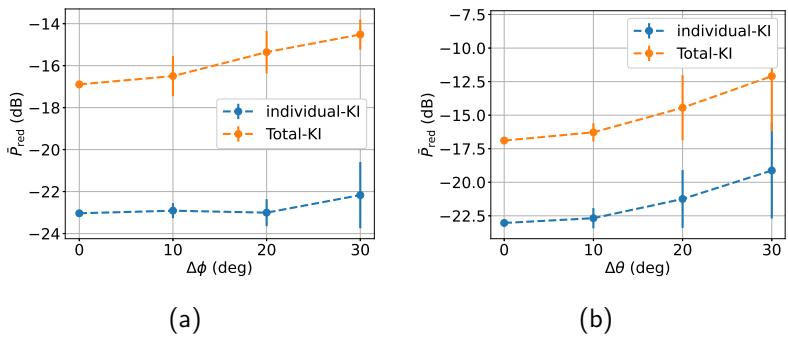

Figure 8: Variation in $\bar{P}_{\mathrm{red}}$ when the (a) azimuth and (b) zenith angles of the primary noise source position were perturbed under the free-field environment.

Next, we added perturbation to the positions of secondary sources in the same manner and performed the same experiments. The standard deviation $\Delta\phi$ or $\Delta\theta$ was selected from $\{0.0, 10.0, 20.0\}$ since it is considered to be smaller than that of the primary source, and each secondary source was perturbed independently. Figure 9 shows the results. The average performance of Individual-KI-FxLMS became worse with the addition of a larger perturbation to the secondary source positions, whereas that of Total-KI-FxLMS did not change markedly. This is because the individual kernel interpolation uses the prior information of secondary source directions, whereas the total kernel interpolation does not. However, Individual-KI-FxLMS still outperformed Total-KI-FxLMS on average even under the perturbation of as much as 20 deg standard deviation.

5.3 Experiments Using Real Data

We perform experiments using real impulse responses measured in a practical environment. The impulse responses between the primary noise and secondary sources and the error microphones and evaluation points were measured one by one at each point using swept-sine signals [22]. The dimensions

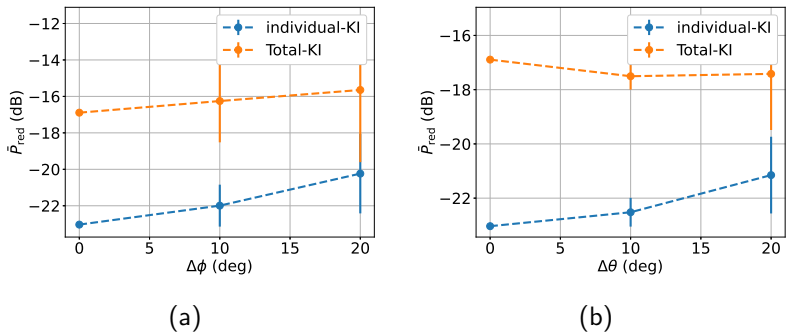

Figure 9: Variation in $\bar{P}_{\mathrm{red}}$ when the (a) azimuth and (b) zenith angles of the secondary source positions were perturbed under the free-field environment.

of the room were approximately 7.0 m × 6.4 m × 2.7 m and the reverberation time T_{60} was about 0.38 s. The primary noise and secondary sources were ordinary closed loudspeakers, and an omnidirectional microphone was used to measure the impulse responses. The error microphones, target region, and primary and secondary sources were placed as described in Section 5.1. We regularly arranged 72 evaluation points inside the two squares with dimensions of 0.6 m × 0.6 m at heights of $z = \pm 0.025$ m. In addition to Individual- and Total-KI-FxLMS, we also implemented conventional FxLMS with the fast block algorithm [8, 7] for comparison. The normalized step-size parameter μ_0 for FxLMS was set to 0.1. The weighting parameters β for Individual- and Total-KI-FxLMS were 2.0 and 0.0, respectively, which were the best ones with respect to $\bar{P}_{\mathrm{red}}$ chosen from $[0.0, 10.0]$ at 1.0 intervals. The other settings were the same as those in the experiments in Section 5.1.

The P_{red} of each algorithm with respect to time is shown in Figure 10. Although μ_0 of FxLMS was chosen for the best performance in terms of $\bar{P}_{\mathrm{red}}$, the P_{red} gradualy increased after 100 s. The individual-KI-FxLMS achieves the highest noise reduction performance among the three methods. The $\bar{P}_{\mathrm{red}}$ achieved by Individual-KI-FxLMS was smaller than that achieved by Total-KI-FxLMS by about 2.5 dB. The power spectrum of the residual noise for the three ANC methods at the evaluation point $(-0.05, -0.05, -0.025)$ m after 750 s is shown in Figure 11. The power spectrum of the primary noise (without ANC) is also shown for comparison, which is smoothed by a Gaussian filter. The noise reduction performance of Individual-KI-FxLMS was higher than that of the other methods in the range of 400-500 Hz.

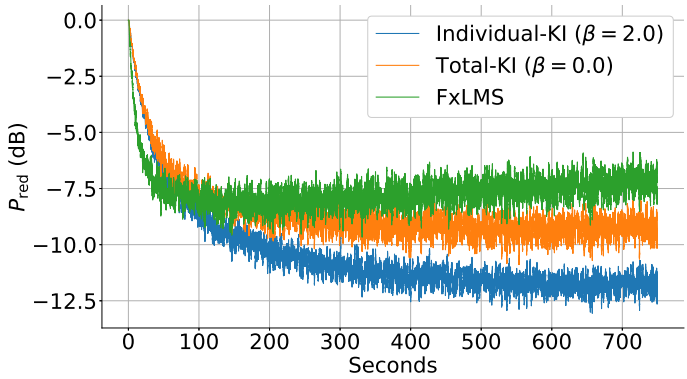

Figure 10: P_{red} values of Individual-, Total-KI-FxLMS, and conventional FxLMS with respect to time obtained using real impulse response data.

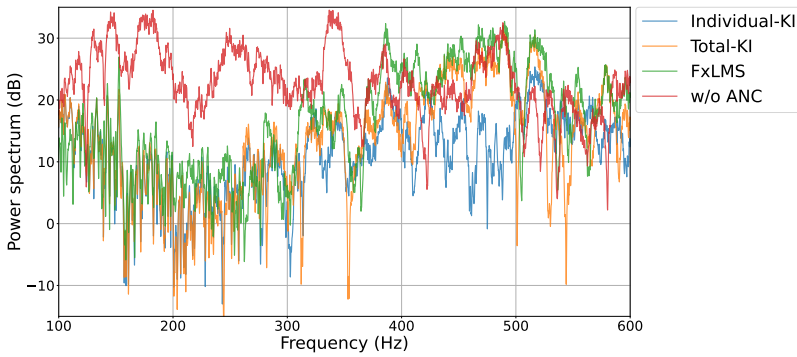

Figure 11: Power spectrum of Individual-, Total-KI-FxLMS, conventional FxLMS, and primary noise (without ANC) at $(-0.05, -0.05, -0.025)$ m.

6 Conclusion

We proposed a spatial ANC method based on the individual kernel interpolation of sound fields. The kernel function with directional weighting makes it possible to incorporate prior information on the source directions. In the previous kernel-interpolation-based ANC, the total sound field is interpolated using a single kernel function with directional weighting only on the primary noise source direction. However, since the total sound field is a superposition of primary and secondary sound fields, which are generated by multiple sources in different directions, the interpolation accuracy will be limited. The proposed individual kernel interpolation estimates the primary and secondary sound

fields separately with directional weighting for each source direction; thus, the interpolation accuracy can be significantly improved. The proposed adaptive filtering algorithm, Individual-KI-FxLMS, is a generalization of the previous Total-KI-FxLMS. In the numerical experiments, we compared the Individual- and Total-KI-FxLMS algorithms under different conditions, which indicated that the proposed method outperforms the previous method in terms of noise reduction performance by appropriately setting the weighting parameter.

References

[1] M. T. Akhtar, M. Abe, and M. Kawamata, "On active noise control systems with online acoustic feedback path modeling", *IEEE Trans. Audio, Speech, Lang. Process.*, 15(2), 2007, 593–600.

[2] J. B. Allen and D. A. Berkley, "Image method for efficiently simulating small-room acoustics", *J. Acoust. Soc. Am.*, 65(4), 1979, 943–50.

[3] K. Arikawa, S. Koyama, and H. Saruwatari, "Spatial Active Noise Control Based on Individual Kernel Interpolation of Primary and Secondary Sound Fields", in *Proc. IEEE Int. Conf. Acoust., Speech, Signal Process. (ICASSP)*, Singapore, May 2022, 1056–60.

[4] B. Bu, C. Bao, and M. Jia, "Design of a Planar First-Order Loudspeaker Array for Global Active Noise Control", *IEEE/ACM Trans. Audio, Speech, Lang. Process.*, 2018, 2240–50.

[5] J. Carmona and V. Alvarado, "Active noise control of a duct using robust control theory", *IEEE Trans. Control Syst. Technol.*, 8(6), 2000, 930–8.

[6] D. Colton and R. Kress, *Inverse Acoustic and Electromagnetic Scattering Theory*, Vol. 93, Springer, 2013.

[7] D. P. Das, G. Panda, and S. M. Kuo, "New block filtered-x LMS algorithms for active noise control systems", *IET Signal Process*, 1(2), 2007, 73–81.

[8] S. Elliott, I. Stothers, and P. Nelson, "A multiple error LMS algorithm and its application to the active control of sound and vibration", *IEEE Trans. Acoust., Speech, Signal Process.*, 35(10), 1987, 1423–34.

[9] H. Ito, S. Koyama, N. Ueno, and H. Saruwatari, "Feedforward Spatial Active Noise Control Based on Kernel Interpolation of Sound Field", in *Proc. IEEE Int. Conf. Acoust., Speech, Signal Process. (ICASSP)*, Brighton, May 2019, 511–5.

[10] H. Ito, S. Koyama, N. Ueno, and H. Saruwatari, "Spatial Active Noise Control Based on Kernel Interpolation With Directional Weighting", in *Proc. IEEE Int. Conf. Acoust., Speech, Signal Process. (ICASSP)*, May 2020, 8399–403.

[11] Y. Kajikawa, W. S. Gan, and S. M. Kuo, "Recent advances on active noise control: open issues and innovative applications", *APSIPA Trans. Signal Inf. Process.*, 1(e3), 2012.

[12] S. Koyama, J. Brunnström, H. Ito, N. Ueno, and H. Saruwatari, "Spatial Active Noise Control Based on Kernel Interpolation of Sound Field", *IEEE/ACM Trans. Audio, Speech, Lang. Process.*, 29, 2021, 3052–63.

[13] S. Koyama, G. Chardon, and L. Daudet, "Optimizing Source and Sensor Placement for Sound Field Control: An Overview", *IEEE/ACM Trans. Audio, Speech, Lang. Process.*, 28, 2020, 686–714.

[14] S. Kuo, S. Mitra, and W.-S. Gan, "Active noise control system for headphone applications", *IEEE Trans. Control Syst. Technol.*, 14(2), 2006, 331–5.

[15] S. M. Kuo and D. R. Morgan, "Active noise control: a tutorial review", *Proc. IEEE*, 86(6), 1999, 943–73.

[16] Y. Maeno, Y. Mitsufuji, P. N. Samarasinghe, N. Murata, and T. D. Abhayapala, "Spherical-harmonic-domain feedforward active noise control using sparse decomposition of reference signals from distributed sensor arrays", *IEEE/ACM Trans. Audio, Speech, Lang. Process.*, 28, 2019, 656–70.

[17] D. Moreau, B. Cazzolato, A. Zander, and C. Petersen, "A Review of Virtual Sensing Algorithms for Active Noise Control", *Algorithms*, 2008, 69–99.

[18] T. Murao and M. Nishimura, "Basic study on active acoustic shielding", *J. Environ. Eng.*, 7(1), 2012, 76–91.

[19] P. A. Nelson and S. J. Elliott, *Active control of sound*, Academic Press, 1991.

[20] H. Sano, T. Inoue, A. Takahashi, K. Terai, and Y. Nakamura, "Active control system for low-frequency road noise combined with an audio system", *IEEE Trans. Speech Audio Process.*, 9(7), 2001, 755–63.

[21] H. Sun, T. D. Abhayapala, and P. N. Samarasinghe, "Time Domain Spherical Harmonic Analysis for Adaptive Noise Cancellation over a Spatial Region", in *Proc. IEEE Int. Conf. Acoust., Speech, Signal Process. (ICASSP)*, 2019, 516–20.

[22] Y. Suzuki, F. Asano, H.-Y. Kim, and T. Sone, "An optimum computer-generated pulse signal suitable for the measurement of very long impulse responses", *J. Acoust. Soc. Am.*, 97(2), 1995, 1119–23.

[23] N. Ueno, S. Koyama, and H. Saruwatari, "Directionally Weighted Wave Field Estimation Exploiting Prior Information on Source Direction", *IEEE Trans. Signal Process.*, 69, 2021, 2383–95.

[24] N. Ueno, S. Koyama, and H. Saruwatari, "Sound Field Recording Using Distributed Microphones Based on Harmonic Analysis of Infinite Order", *IEEE Signal Process. Lett.*, 25(1), 2018, 135–9.

[25] E. G. Williams, *Fourier Acoustics: Sound Radiation and Nearfield Acoustical Holography*, Academic Press, 1999.

[26] J. Zhang, T. D. Abhayapala, W. Zhang, P. N. Samarasinghe, and S. Jiang, "Active Noise Control Over Space: A Wave Domain Approach", *IEEE/ACM Trans. Audio, Speech, Lang. Process.*, 2018, 774–86.